Large Eddy Simulation of Flow and Heat Transfer Around Two Square Cylinders in a Tandem Arrangement

F. Duchaine, M. Boileau, Y. Sommerer, Thierry Poinsot

F. Duchaine[1]
CERFACS,
42 Avenue Coriolis,
Toulouse Cedex 01 31 057, France
e-mail: florent.duchaine@cerfacs.fr

M. Boileau[2]
CERFACS,
42 Avenue Coriolis,
Toulouse Cedex 01 31 057, France

Y. Sommerer
AIRBUS Operations,
EDET30 Engine and Nacelle Integration,
316 Route de Bayonne,
Toulouse Cedex 09 31060, France

T. Poinsot
IMF Toulouse,
INP de Toulouse and CNRS,
Toulouse 31400, France

Large Eddy Simulation of Flow and Heat Transfer Around Two Square Cylinders in a Tandem Arrangement

This paper presents a large eddy simulation (LES) of flow and heat transfer in a tandem configuration of two square cylinders at moderate Reynolds number ($Re = 16,000$). Compressible LES on a hybrid mesh is used to predict the flow structure and the heat transfer at the wall. The goals of this work are to analyze the flow and the heat transfer around a tandem arrangement of two inline square cylinders as well as to propose a LES approach that can be applied to convective heat transfer problems in industrial configurations. The meshing strategy allows to resolve the flow field until the viscous sublayer with y^+ of the order unity. The wall adapting linear eddy model is chosen to model the subgrid turbulent viscosity. Aerodynamics results are validated versus experimental measurements performed on isolated cylinders and on tandem configurations. The main flow structures responsible for heat transfer are analyzed. Finally, heat transfer around both cylinders of the tandem is described. [DOI: 10.1115/1.4027908]

Keywords: tandem cylinder, heat transfer, large eddy simulation

1 Introduction

Forced convection heat transfer around multiple bluff bodies is of practical engineering importance and has attracted a considerable amount of interest in the recent past: Industrial systems exhibit complex geometries and flows where simple configurations with a single bluff body in a steady flow are rarely encountered. Usually, the bluff bodies (representative of a specific system or equipment) are of different sizes and have complex shapes. They can be placed in the wake of other bodies, leading to either an increase or a decrease of their cooling. An application of such flows is found in aeronautical engine compartments where the thermal behavior of equipments like valves, electrical harnesses, or ducts have to be studied in order to guarantee that they never exceed their maximum allowable temperature in the whole aircraft's flight envelope.

In order to evaluate the precision of heat transfer computations, it is convenient to study a simplified configuration. Accordingly, we aim to increase our understanding of the flow around a heated inline square cylinder arrangement in a colder flow at moderate Reynolds number ($Re = 16{,}000$). The most striking phenomenon in flows past multiple bluff bodies is the generation of a complex structure by the mutual interactions among the wakes behind the bodies. These wake interactions subsequently lead to vortex shedding. Heat transfer and the resulting thermal field is controlled by this complex unsteady flow.

Many studies have been reported to characterize the aerodynamics [1–3] as well as the heat transfer [4,5] of single square-section cylinders. The flow over two inline square cylinders has also been characterized in the last two decades [6–14]. Several center-to-center distances, size-ratios, and Reynolds numbers have been investigated in these studies. Only few studies have addressed heat transfer in tandem cylinders and most of them were limited to low Reynolds number cases [13,15–17].

The aim of the present study is to analyze the flow and the heat transfer around a tandem arrangement of two inline square cylinders, using a high fidelity LES at moderate Reynolds number ($Re = 16{,}000$). Due to the value of the Reynolds number, direct numerical simulation (DNS) of the flow would be numerically too expensive. Recent progress in LES [18–20] and the continuously increasing computer power offered by the newly developed parallel computer architectures, allow to accurately predict turbulent flows in complex geometries [21–24]. As a result, LES is a good candidate to predict unsteady wake flows. For such problems, special attention must be paid to the near-wall modeling. While it is computationally intensive for high Reynolds number flows, using enough grid resolution with a proper subgrid model, LES can behave like a DNS when approaching the wall. For most industrial internal flows, structured grids are often difficult to generate and unstructured meshes composed of tetrahedral elements are easy to set up. Unstructured grid technique is thus retained for the present study. For the same spatial resolution, an unstructured grid is usually more expensive and less accurate than a calculation on a structured grid. As a result, unstructured grids must be generated carefully, especially when dealing with convective heat transfer.

Aerodynamics are validated using experimental results and then used to understand the dynamics of the flow responsible for heat loads. As the bibliography does not allow a complete validation, the comparisons are made with several experimental isolated and tandem configurations with different Reynolds number and topology. This work constitutes a first attempt to characterize the heat transfer by convection in this academic wake interaction configuration at moderate Reynolds number. Thus, heat transfer results constitute a database for comparisons with industrial methodologies such as unsteady Reynolds averaged Navier–Stokes simulation.

The paper is organized as follows. First, the LES solver is presented. Then the tandem configuration is introduced. Section 4 presents the results. Aerodynamics is first characterized and

[1]Corresponding author.
[2]Present address: Laboratoire EM2C-CNRS, Ecole Centrale Paris, Châtenay Malabry 92295, France.

validated. Finally, thermal results are exposed and compared with experimental results on isolated cylinders.

2 Numerical Approach

2.1 Governing Equations and LES Models. The initial governing equations solved are the unsteady compressible Navier–Stokes equations that describe the conservation of mass, momentum and energy. For compressible turbulent flows the primary variables are the density ρ, the velocity vector u_i, and the total energy $E \equiv e_s + 1/2 u_i u_i$. The fluid follows the ideal gas law, $P = \rho R T$ and $e_s = \int_0^T c_p dT - P/\rho$, where e_s is the sensible energy, P the pressure, T the temperature, c_p the fluid heat capacity at constant pressure, and r is the mixture gas constant. The LES solver takes into account changes of heat capacity with temperature using tabulated values of c_p. The viscous stress tensor and the heat diffusion vector use classical gradient approaches. The fluid viscosity follows Sutherland's law and the heat diffusion coefficient follows Fourier's law. The Prandtl number of the fluid is taken as $\mathrm{Pr} = 0.72$. The application of the filtering operation to the instantaneous set of compressible Navier–Stokes transport equations yields the LES transport equations [20] which contain subgrid scale (SGS) quantities that need modeling [18,25]. The unresolved SGS stress tensor is modeled using the Boussinesq assumption [26,27]. The wall adapting local eddy (WALE) model [28] is chosen to model the SGS viscosity. This model is designed to provide correct levels of turbulent viscosity down to the wall and no wall model is required. The SGS energy flux is modeled using a SGS turbulent heat conductivity λ_t obtained from ν_t by $\lambda_t = \bar{\rho}\,\nu_t\, c_p/\mathrm{Pr}_t$ where the turbulent Prandtl number is kept constant at $\mathrm{Pr}_t = 0.7$. The WALE subgrid model is used in conjunction with no-slip wall conditions.

2.2 Numerical Schemes. The parallel LES code [29–31] solves the full compressible Navier–Stokes equations using a cell--vertex/finite element approximation and Taylor–Galerkin weighted residual central distribution scheme [32] on unstructured grids. This explicit scheme provides third-order accuracy on hybrid meshes and satisfies low-dissipation requirements of LES applications [33]. The explicit time step Δt is imposed by the Courant–Friedrichs–Lewy number condition, $\mathrm{CFL} = ((U + c)\Delta t/\Delta x) = 0.7$, where Δx is the size of the grid cell while U and c are the flow and sound local velocities, respectively.

3 Configuration

3.1 Problem Statement and Boundary Conditions. The three-dimensional computational domain consists of two inline square cylinders confined in the middle of a channel of length $L = 32D$ and height $h = 15D$ (Fig. 1). The two cylinders are identical in size, with square cross sections of $D \times D$, where D is the characteristic length of the problem. The vertical dimension of the channel is fixed in order to match a blockage ratio D/h of 6.6% [14]. Inlet and outlet boundary conditions are placed sufficiently far from the tandem to prevent boundary from influencing the flow around the cylinders and the near-wake. The size of the cylinders in the transverse direction (Z on Fig. 1) is $E = 2D$ and a periodic condition is imposed on the lateral sides in order to mimic a large spanwise. This span size is chosen in order to reduce the computational cost of the simulation according to industrial constraints. It is known from the literature that a transverse size of almost $4D$ is required to capture detailed features of such flows [34]. Nevertheless, in the present configuration, a spanwise of $2D$ appears sufficient to reproduce the first order statistics of the average fields. As the blockage factor D/h is rather small, the effect of the boundary layers that develop on the channel walls on the flow around the cylinders is neglected. Adiabatic slip conditions are imposed on the walls of the channel. Isothermal conditions are applied to the cylinder boundaries. A laminar uniform

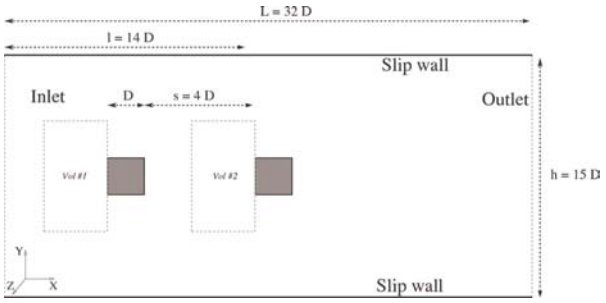

Fig. 1 Global view of the computational domain and boundary conditions. Vol. #1 and Vol. #2 refer to volumes of size $2D \times 4D$ in *XY* plane used for diagnostics.

flow is imposed at the inlet of the domain, using the Navier–Stokes Characteristic boundary condition formalism (NSCBC) [35]. Static pressure is enforced at the outlet boundary in characteristic NSCBC form.

3.2 Meshing Strategy. As shown in Fig. 2, the grid is coarse far from the cylinders ($\Delta x/D = 0.5$), moderately refined in the near-wake region ($\Delta x/D = 0.05$) and strongly refined close to the cylinders ($\Delta x/D \leq 0.04$). The discretization of the cylinder surfaces is set to $\Delta x/D \leq 0.008$ corresponding to typical values of y^+ of less than unity on a large part of the walls. This refinement is expected to be sufficient to capture the turbulent flow generated by the Kelvin–Helmholtz instability in the detached upper and lower shear layers of the cylinders and by the Von-Karman instability in the tandem wake.

The WALE model [28] is able to recover the proper y^3 damping scaling for the eddy viscosity at the wall without any damping function nor dynamic procedure. However, to provide the right viscous stress and heat flux at the wall, the grid cells adjacent to the wall must be inside the viscous sublayer. This condition requires a high density of very small grid cells close to the wall (i.e., large grids and small time steps following) which leads to expensive simulations. When the boundary layer is explicitly resolved, using prismatic layers close to wall surfaces is more efficient than using tetrahedra. First, quadrilateral faces normal to the wall provide good orthogonality and grid-clustering capabilities which are well suited to thin boundary layers, whereas the triangulation in the tangential direction allows for more flexibility in surface modeling. Second, for same spatial resolution in the normal direction, the prismatic layer approach uses less elements and leads to a higher minimum cell volume than the full tetrahedral

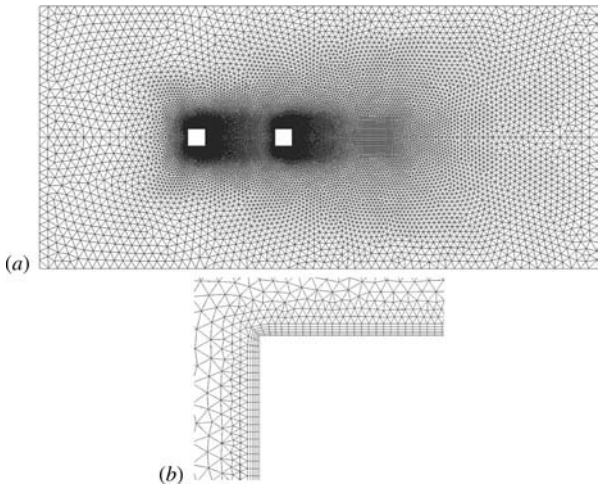

Fig. 2 (*a*) Side view of the computational grid. (*b*) Zoom on the five layers of prismatic elements at the surface of the cylinders.

grid approach because prismatic elements can have a large aspect ratio. Thus, the near-wall region has been meshed using five layers of prismatic elements (Fig. 2) where the height of the layer, Δh, is smaller than the size of their triangular basis, Δx. To avoid numerical errors in the prismatic layers, the aspect ratio of the thinnest layer (inner layer adjacent to the wall) has been limited to $\Delta x/\Delta h = 4$ (far from the cylinder edges) or 3 (near the edges). The stretching ratio between the height of an inner layer to the adjacent outer layer has been set to 1:13, leading to a prism aspect ratio of $\Delta x/\Delta h = 1.83 - 2.45$ in the outer layer. The proper height of the inner prism layer ($\Delta h/D$) has been determined by a mesh convergence study based on the global Nusselt number Nu for an isolated square cylinder compared to the experimental correlation of Igarashi [4]. A previous study has shown that $\Delta h/D \leq 0.002$ is required to match the empirical Nusselt number for a Reynolds number of Re = 22,050 [31]. Using this mesh constraint in the near-wall region and the mentioned sizes in other regions leads to a grid of 3×10^6 nodes (12×10^6 cells).

3.3 Physical Parameters. The tandem wall condition corresponds to a uniform temperature $T_{\text{wall}} = 330\text{K}$ while the upstream flow is at $T_\infty = 300\text{K}$. Since this temperature jump is small, the fluid temperature is expected to behave mostly as a passive scalar having a negligible effect on the flow hydrodynamics. However, the variation of the temperature in the boundary layer induces a variation of the fluid transport properties which must be accounted for. The Reynolds number $\text{Re} = U_\infty D/\nu$ has been calculated from the kinematic viscosity $\nu = \mu/\rho$ taken at the film temperature $T_\text{f} = \frac{1}{2}(T_\infty + T_{\text{wall}})$. Computing ν from T_∞ or T_{wall} instead of T_f would result in 10% error on the Reynolds number, whose target is fixed to Re=16,000.

In the case of a low Mach number flow ($M = U/c \ll 1$), the number of temporal iterations N_{ite} needed to simulate one flow time (one shedding period or one flow through time) can be approximated by $N_{\text{ite}} \approx D/(M\,CFL\Delta x)$, where D is the characteristic length scale. In order to avoid a drastic increase in the number of iterations N_{ite} when M is small, it is judicious to maximize the Mach number while maintaining low compressible effects. Thus, the upstream Mach number is set to $M_\infty = 0.105$ so that the maximum Mach number does not exceed 0.2 in the regions of highest velocity. Giving that Mach number scaling, using a compressible formulation for an incompressible anisothermal flow has advantages: On the one hand, it captures intrinsically the variation of density with temperature, on the other hand, the problem can be solved by an explicit numerical scheme which is well adapted to massively parallel computing. The diameter of the cylinders is then deduced from the values of the Mach and Reynolds numbers: $D = 7.5\text{mm}$. The simulation of one period of the vortex shedding requires approximately 1470 central processing unit (CPU) hours on an IBM JS21 PowerPC cluster (2.2 Peak Tflops on 224 computing cores).

The physical parameters of the simulation are summed up in Table 1. In the following, lengths are normalized by D, velocities by the upstream velocity U_∞ and times by the convective time $t_\text{c} = D/U_\infty$.

3.4 Experimental Data. For a given Reynolds number, the flow pattern around a tandem of cylinders depends strongly on the spacing between the centers of the cylinders [10,14]. At a so-called critical spacing, the flow pattern may dramatically change from one stable mode to another. The resulting surface pressure, drag coefficient, and vortex shedding frequency alter abruptly to reflect the mode change. In the range of Reynolds numbers of interest, the first mode is stable when $s < 3D$. The first mode is characterized by a reattachment of the separated shear layers generated by the upstream cylinder edges on the lateral faces of the downstream cylinder. Two counter-rotating recirculation zones are formed in the interspace between the cylinders. When the distance s becomes greater than $3D$, the shear layers are convected between the cylinders and periodical vortex shedding from each of the cylinders occurs (mode 2). For an interspace $s = 4D$ and a Reynolds number of 16,000, the literature [10,14] describes a pattern corresponding to the second mode.

Table 1 Physical parameters of the simulation

Cylinder diameters	$D = 7.5$ mm
Upstream velocity	$U_\infty = 36.6$ ms^{-1}
Upstream temperature	$T_\infty = 300$ K
Upstream Mach number	$M_\infty = 0.105$
Cylinder temperatures	$T_{\text{wall}} = 330$ K
Film temperature	$T_{\text{ref}} = 315$ K
Reynolds number	Re=15,989
Outlet pressure	$p_{\text{out}} = 101,325$ Pa

Table 2 Experimental databases used for comparisons with the LES. IC stands for isolated cylinder, $C_\text{p}(s)$ and Nu(s) are the pressure coefficient and Nusselt number profiles on the cylinder surfaces, $\overline{C_\text{D}}$ is the drag coefficient, St is the Strouhal number, $\overline{\text{Nu}}$ is the integral of Nu(s) over the cylinders, $u(s)_{\text{BL}}$ and $u'(s)_{\text{BL}}$ are the profiles of streamwise velocity and streamwise velocity fluctuation in the boundary layer of the cylinders, $u(s)_\text{W}$ and $u'(s)_\text{W}$ are the profiles of streamwise velocity and streamwise velocity fluctuation in the wake of the cylinders.

Reference	Re	Configuration	Data
[1]	20,000	IC	$C_\text{p}(s)$
[4]	18,500	IC	$C_\text{p}(s) - \text{Nu}(s) - \overline{\text{Nu}}$
[2]	21,400	IC	$\overline{C_\text{D}} - u(s)_{\text{BL}} - u'(s)_{\text{BL}}$ $u(s)_\text{W} - u'(s)_\text{W}$
[3]	21,400	IC	$\overline{C_\text{D}}$
[5]	19,200	IC	$\overline{\text{Nu}}$
[7]	33,200	$s = 4D$	$\overline{C_\text{D}}$
[8]	10,000	$s = 3D$	$\overline{C_\text{D}} - u(s)_\text{W} - u'(s)_\text{W}$
[10]	16,000	$s = 4D$	$\overline{C_\text{D}} - \text{St}$
[14]	16,000	$s = 4D$	$\text{St} - u'(s)_\text{W}$

The validation of the LES is achieved by comparing aerodynamical data with experimental results obtained on isolated cylinders and on tandem configurations. Indeed, as some quantities are not present in experimental databases for the tandem configuration, cross validation with different experiments is made. Moreover, in the configuration studied here, the simulation suggests that the upstream cylinder behaves almost like an isolated cylinder, allowing comparison with experimental data on isolated cylinders.

As no thermal measurement is available for tandem cases at moderate Reynolds numbers, heat transfer results are compared with isolated cylinder experiments. Experimental studies used for comparisons are summarized in Table 2.

In the following, the results are analyzed in the normalized form presented in Table 3. The time average, denoted by $\bar{\phi}$, is performed by averaging arithmetically any time-dependent flow variable $\phi(t)$. The corresponding fluctuation, noted $\phi\prime$, is the root mean square value of $\phi(t)$. In order to extract statistical data from the average LES solutions, every three-dimensional field is averaged in the spanwise (z) direction which can be considered as statistically homogeneous. Figure 3 displays the positions of the cutting lines used to compare computational and experimental profiles.

4 Results and Discussion

4.1 Aerodynamics Results

4.1.1 Flow Characterization. The flow is characterized by vortex shedding due to the Kelvin–Helmholtz instabilities in shear layers produced by the upstream edges of both cylinders and by a

Table 3 Dimensionless forms of the LES results. τ_{wall} is the wall shear stress. F_D is the drag force. q_{wall} is the conductive flux at the wall. λ_{wall} is the thermal conductivity at the wall.

Spatial coordinates	x/D and y/D
Velocity	u/U_∞ and v/U_∞
Pressure coefficient	$C_p = (p - p_\infty)/(\frac{1}{2}\rho_\infty U_\infty^2)$
Friction coefficient	$C_f = \tau_{wall}/(\frac{1}{2}\rho_\infty U_\infty^2)$
Drag coefficient	$C_D = F_D/(\frac{1}{2}\rho_\infty U_\infty^2 ED)$
Nusselt	$\mathrm{Nu} = q_{wall} D/(\lambda_{wall}(T_{wall} - T_\infty))$

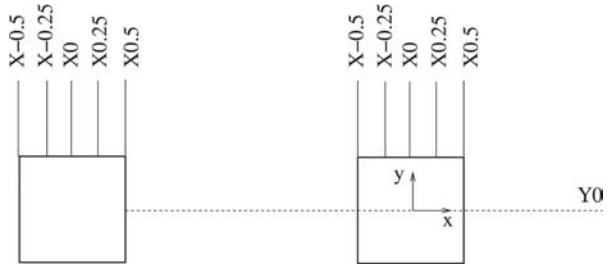

Fig. 3 Definition of the cutting lines used to display the profiles

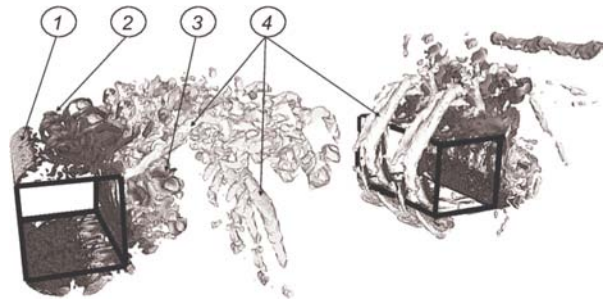

Fig. 4 Instantaneous isosurface of Q-criterion colored by the temperature (lower temperature in white and higher temperature in dark)

Von-Karman street in the wake of the tandem (Fig. 4). The isosurface of the Q-criterion [36] on Fig. 4 shows the complex three-dimensional organization of the flow around the cylinders and in their wake. The vorticity layers (flag number 1 of Fig. 4) generated by the upstream cylinder destabilize in the near field of the lateral faces of this obstacle (flag number 2) and form three-dimensional coherent structures (flag numbers 3 and 4). In conjunction with the alternate vortices (flag number 3), longitudinal structures (flag number 4) are formed in the wake of the first cylinder and are convected downstream. The downstream cylinder disturbs the development and convection of all these structures so that the wake of the upstream cylinder participates actively to heat transfer on the second one. The LES reproduces the behavior of mode 2 (Figs. 4 and 5) as expected from the bibliography descriptions [10,14].

To characterize the vortex shedding from both cylinders, a pressure probe is placed on the top face of each obstacle. As mentioned by Ref. [10], the registered signals are synchronized meaning that the shedding of vortices is in phase for both cylinders. The amplitude of the pressure oscillations is more important for the downstream cylinder. The Strouhal number $\mathrm{St} = fD/U_\infty = 0.125$, with f the frequency of the oscillations of the pressure signals, is close to the experimental values obtained by Ref. [10] 0.126 and Ref. [14] 0.128. These results suggest that the shedding mechanism is well reproduced by the LES. The sequence of images provided on Fig. 5 represents the temporal evolution of the vorticity during one period of the vortex shedding. The second mode is clearly illustrated on this sequence: The vorticity generated by the upstream cylinder flows through the obstacles and interacts with the upstream and lateral faces of the second cylinder. Moreover, the synchronization between the vortex shedding is illustrated. An additional information is available from Fig. 5: The vortices generated by the upstream cylinder feed the recirculation zones on the lateral faces of the downstream cylinder. The resulting vortices are more energetic than the ones created by an isolated cylinder, explaining the difference in amplitude of pressure signals mentioned before.

The mean axial velocity field (Fig. 6) allows the identification of the recirculation zones around the cylinders. The recirculation behind the upstream cylinder is more spread out in the transverse direction (y axis) than the one of the downstream cylinder. It also has a lower intensity in terms of reverse axial velocity. The axial lengths of these recirculation zones are almost the same. They are present on the lateral faces of the upstream cylinder and absent from the downstream cylinder. Second-order moments of

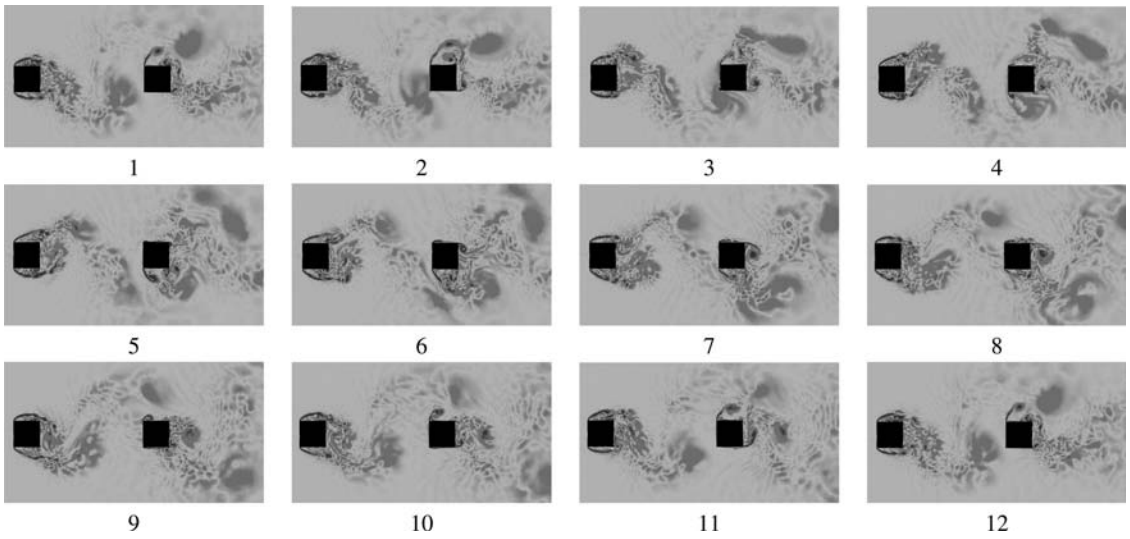

Fig. 5 Evolution of the vorticity around the tandem during one shedding period on the middle plane

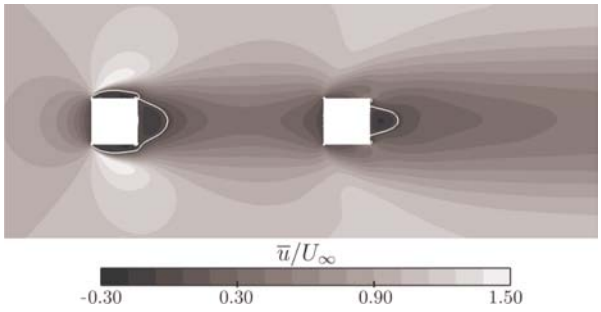

Fig. 6 Isocontours of streamwise time averaged velocity $\bar{u}/U_\infty$ and isoline of zero axial velocity

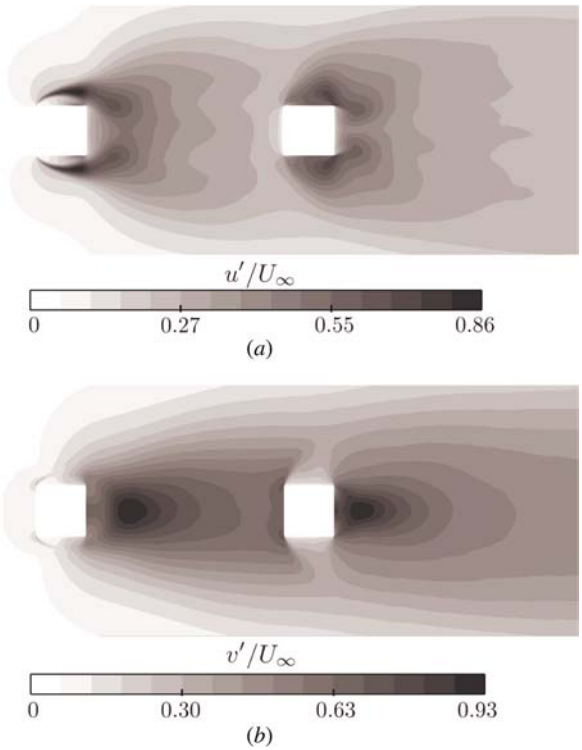

Fig. 7 (*a*) Isocontours of streamwise fluctuating velocity u'/U_∞, (*b*) isocontours of transverse fluctuating velocity v'/U_∞

longitudinal and transverse velocity (Fig. 7) underline the topological differences between the flow fields around the cylinders. Axial velocity fluctuations in the shear layers generated by the edges of the downstream cylinder are more spread out than for the upstream cylinder and their intensities are lower. Indeed, shear layers generated by the upstream cylinder stay mostly two-dimensional and oscillate only with periodic vortex shedding. On the contrary, shear layers generated by the downstream cylinder are submitted to strong oscillations due to incoming vortices shed by the upstream cylinder. Hence, the shear layers oscillate with a large amplitude before impacting the lateral faces of the cylinder and being destroyed (see Fig. 5). The size and localization of the zones of maximum transverse velocity fluctuations show that the vortices generated by the downstream cylinder form closer to its backward face than for the upstream cylinder. This observation explains the difference of intensity of the recirculation zones behind the cylinders. The global structure of the flow matches previously published studies [10,14]. Section 4.1.2 aims at validating the simulation with more quantitative aerodynamic quantities.

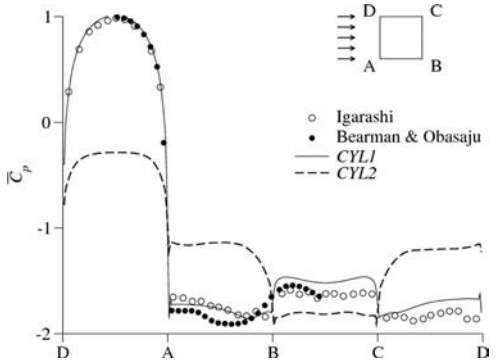

Fig. 8 Time-averaged profiles of pressure coefficient, $\bar{C}_p$ around the two cylinders of the LES compared to isolated cylinder [1,4]

4.1.2 Aerodynamic Validation. Wall quantities are first compared to experimental measurements of Refs. [1] and [4]. Then, first- and second-order aerodynamic moments on transverse and longitudinal cuts (Fig. 3) are compared to experimental data from Refs. [2] and [3] for an isolated cylinder and Ref. [14] for a tandem configuration.

Wall quantities: Mean pressure coefficient $\bar{C}_p$ profiles on the two cylinders are plotted on Fig. 8. The pressure coefficient profile of the upstream cylinder fits the measurements of isolated cylinders on upstream (A-D) and lateral faces (A-B, C-D). Compared to an isolated cylinder, the downstream face (B-C) of the first cylinder seems to be exposed to a less intensive pressure force. Nevertheless, from the aerodynamic force point of view, the upstream cylinder (solid line) can be considered as an isolated cylinder. On the contrary, the downstream cylinder (dashed line) exhibits drastic changes in the $\bar{C}_p$ distribution: Its upstream face (A-D) is submitted to an aspiration force oriented in the opposite direction of the main flow which created by the wake of the first cylinder. This leads to a negative mean pressure coefficient. Then, lateral faces (A-B, C-D) are exposed to smaller pressure forces than an isolated cylinder. Finally, the pressure force acting on the downstream face (B-C) in the opposite direction of the flow is stronger than in the case of an isolated cylinder.

To characterize the flow field resolution in the near-wall region, the transverse nondimensional coordinate of the first wall cell y^+ is used:

$$y^+ = \frac{u_\tau}{\nu}\Delta h \tag{1}$$

where Δh is the first wall cell height and u_τ is the friction velocity defined by

$$u_\tau = \sqrt{\frac{\tau_{\text{wall}}}{\rho}} \tag{2}$$

In Eq. (2), τ_{wall} is the wall shear stress expressed by considering that the first computing cell belongs to the viscous sublayer

$$\tau_{\text{wall}} = \mu_{\text{wall}}\frac{\partial \bar{u}}{\partial y} \approx \mu_{\text{wall}}\frac{\bar{u}_h}{\Delta h} \tag{3}$$

where u_h is the velocity of the nearest fluid point to the wall and μ_{wall} is the dynamic viscosity of the fluid at the wall. y^+ profiles (Fig. 9(*a*)) confirm that the LES resolves the flow field down to the viscous sublayer ($y^+ < 6$) for both cylinders.

The distributions of the mean friction coefficient $\bar{C}_f$ defined in Table 3 for the two cylinders are shown in Fig. 9. Note that in order to better understand the flow topology around the cylinders, the mean friction coefficient $\bar{C}_f$ is algebraic. It has a negative

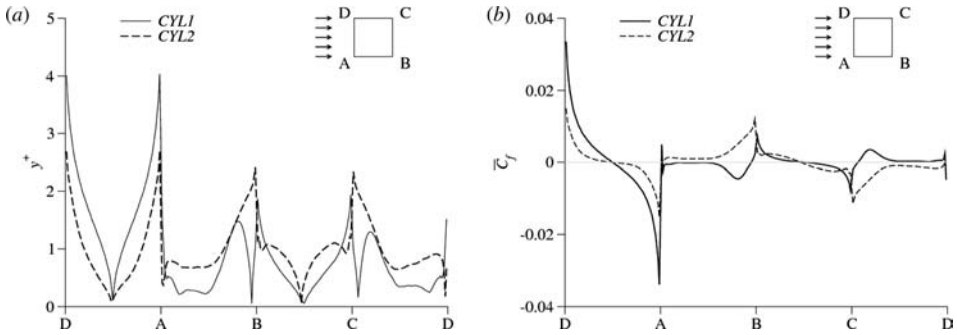

Fig. 9 (*a*) Time-averaged wall Reynolds number y^+ and (*b*) time-averaged profiles of friction coefficient C_f around the two cylinders

Table 4 Spatially and temporally averaged aerodynamic wall variables. The experiments of Refs. [2] and [3] deal with isolated cylinders.

	$\bar{C}_D$		$\bar{y}^+$	
	CYL 1	CYL 2	CYL 1	CYL 2
Present LES	2.199	1.42	0.93	0.97
LES [31]	2.26	—	—	—
Reference [7]	2.47	1	—	—
Reference [2]	2.16	—	—	—
Reference [3]	2.1	—	—	—
Reference [8]	—	2	—	—
Reference [10]	1.83	0.82	—	—

value when the mean velocity of the nearest fluid point to the wall $\bar{u}_h$ has the direction of D to A, A to B, B to C, and C to D. Otherwise, it is positive. The global forms of $\bar{C}_f$ on the upstream faces (A-D) are identical. Nevertheless, the upstream cylinder is subject to a friction at least twice higher than that of the downstream cylinder. The friction coefficient on lateral faces (A-B, C-D) of the upstream cylinder is typical of an isolated cylinder: The separated regions generated by the upstream edges of the cylinder imply a friction almost zero which acts in the opposite direction of the main fluid flow due to the recirculation zones (negative values of $\bar{C}_f$ on A-B and positive on C-D). The peak in the friction coefficient on the lateral faces near the downstream edges of the first cylinder is linked to the interaction between the shear layer and the wall as well as to the beginning of the back flow of vortices along the wall. For the second cylinder, the strong oscillations of the lateral shear layers cause an intermittence during which the lateral recirculation zones vanish or are convected downstream. Without the protection of the recirculation bubbles, the lateral faces are directly exposed to the friction of the main flow. The friction coefficient is then higher and has the same sign as the flow direction ($\bar{C}_f$ positive on A-B and negative on C-D). The peak in the friction coefficient on the lateral faces near the downstream edges of the second cylinder is due to vortices oscillating behind the downstream face (B-C) that tend to propagate upstream on a short distance. Finally, the friction of the downstream face is higher for the second cylinder. This difference is due to the closest proximity of vortices for the second cylinder mentioned above.

The mean wall quantities $\bar{C}_D$ and $\overline{y^+}$, averaged in space and time, are given in Table 4. As in the experimental results [7], the drag coefficient of the downstream cylinder is lower than that of the upstream cylinder. The drag coefficient of the upstream cylinder obtained by the present simulation matches drag coefficients obtained on isolated cylinders [2,3]. The discrepancies between present drag coefficients and those obtained by Refs. [7] and [10] can be explained by the differences in Reynolds number, blockage ratio as well as inlet free stream turbulence, or on modelization hypothesis such as mesh resolution and spanwise size E of the cylinders.

Axial velocity profiles in the neighboring of the cylinders: Figure 10 shows a comparison between mean axial velocity $\bar{u}/U_\infty$ on the upper face (C-D) of each cylinder with the experimental data of Ref. [2] for an isolated cylinder. The numerical results concerning the upstream cylinder agree with the experimental profiles. For the first obstacle, the velocity levels match the experimental results. Nevertheless, the velocity of the recirculating flow is lower and a slight shift is observed in the position of the shear zone located far away from the wall in the computation. Due to the wake of the upstream cylinder, the velocity profiles of the downstream cylinder exhibit a deficit of velocity (Fig. 10,

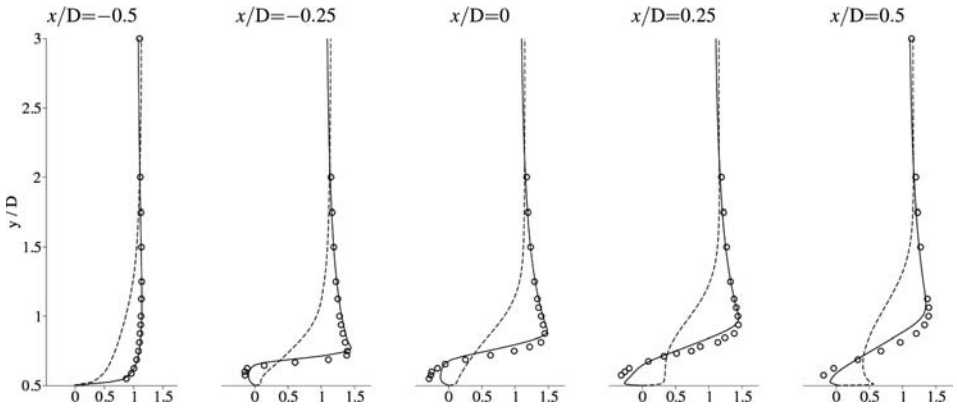

Fig. 10 Transverse profiles of time-averaged streamwise velocity, $\bar{u}/U_\infty$, on the upper face of the cylinders (cuts $X/D = -0.5$ to $X/D = 0.5$ of Fig. 3): experimental results from an isolated cylinder [2] (○), upstream (–) and downstream (– –) cylinders of the present LES

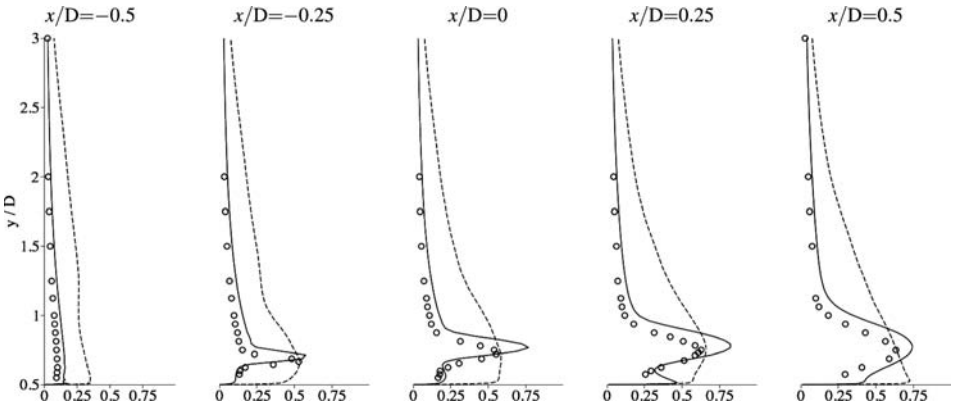

Fig. 11 Transverse profiles of time-averaged streamwise velocity fluctuation, u'/U_∞, on the upper face of the cylinders (cuts $X/D = -0.5$ to $X/D = 0.5$ of Fig. 3): experimental results from an isolated cylinder [2] (○), upstream (–) and downstream (– –) cylinders of the present LES

dashed line). The velocity gradients are smaller for the second cylinder. As already mentioned (Fig. 6), axial velocity profiles show that there is no recirculation zone on lateral faces of the downstream cylinder. The inflection of the last two profiles ($x/D = 0.25$ and $x/D = 0.5$) is due to upstream propagation of vortices coming from the downstream face (Fig. 9).

Profiles of fluctuating axial velocity in the neighboring of the cylinders: Figure 11 shows a comparison between profiles of fluctuating streamwise velocity u'/U_∞ on the upper face (C-D) of each cylinder with the experimental data of Ref. [2] for an isolated cylinder. The upstream cylinder behaves like an isolated cylinder: The highest levels of velocity fluctuation are located in the shear layer identified on Fig. 10. For the first two profiles ($x/D = -0.5$ and -0.25), the shapes and the levels of the profiles match experimental data. An overestimation of the maximum level of the velocity fluctuations is observed on the following profiles. It is interesting to note that the fluctuation levels are well reproduced on the recirculation zone (i.e., $\bar{u} < 0$), indicating that the flow dynamic is well captured by the simulation in the near-wall region. As the downstream cylinder is immersed in the wake of the first one, the global level of velocity fluctuations is higher. In accordance with a lower gradient of the mean velocity $\partial\bar{u}/\partial y$, the peaks of fluctuations observed on the profiles $x/D = -0.25$, $x/D = 0$ and 0.25 are spread out compared to the upstream cylinder. This peak is no more visible on the last profile ($x/D = 0.5$) due to the upstream propagation of vortices coming from the downstream face, as explained before (Fig. 9).

Longitudinal profiles in the wake of the cylinders: The mean axial velocity profile along the symmetry plane of the configuration is compared to the measurements of Ref. [2] for an isolated cylinder and of Ref. [8] for a tandem (Fig. 12(*a*)). For the downstream cylinder, the results obtained by the simulation are not in a good agreement with the experimental data of Ref. [8]. Nevertheless, the Reynolds numbers of the computation and of the experiments are not the same (16,000 versus 10,000, respectively) and the interspace distance between the cylinder also differs ($s = 4D$ versus $s = 3D$, respectively). Moreover, it is important to note that the experimental results of Ref. [8] for an isolated cylinder in terms of recirculation zone and velocity deficit relative to the upstream velocity in the wake do not match the results of Ref. [2]. The presence of the second cylinder has an important impact on the mean axial velocity behind the first cylinder. Compared to an isolated cylinder, the length and the intensity of the recirculation zone are greatly reduced. In contrast, the size and the intensity of the recirculation zone of the downstream cylinder are comparable to an isolated cylinder. The velocity deficit relative to the upstream velocity far away in the wake of the cylinders ($x/D > 3$) is more important in the case of the tandem than for an isolated cylinder.

Figures 12(*b*) and 12(*c*) show the axial and transverse velocity fluctuations on the duct centerline compared to the experimental data of Ref. [2] for an isolated cylinder and of Refs. [8] and [14] for tandems. As observed for the first moment of the axial velocity, the fluctuations obtained by LES on the upstream cylinder match the measurements on an isolated cylinder. The forms and the levels of the profiles obtained by Ref. [14] in the wake of the upstream cylinder are not reproduced by the simulation: The peaks on u'/U_∞ and v'/U_∞ occur more downstream in the measurements of Ref. [14] than in the data of Ref. [2] and in the present simulation. Compared to an isolated cylinder, the levels of u'/U_∞ and v'/U_∞ obtained by the LES are overestimated and the peak of fluctuation is localized more upstream in the flow. Concerning the wake of the downstream cylinder, the streamwise velocity fluctuations predicted by the simulation are more important than the data reported by Ref. [8]. As mentioned for the mean axial velocity profile, the results obtained by Ref. [8] on an isolated cylinder are lower than the results of Ref. [2].

On the one hand, the simulation predicts higher axial fluctuations in the wake of the upstream cylinder than in the wake of the second. On the other hand, transverse fluctuations are almost equal in both wakes. As a result, the first cylinder generates more turbulent kinetic energy than the second. Moreover, the peak of turbulent kinetic energy behind the obstacles is closer to the downstream face for the second cylinder than for the upstream cylinder. Finally, the upstream face of the downstream cylinder ($x/D = -0.5$) exhibits a peak of v'/U_∞ linked to the interaction of the vortex shedding generated by the upstream cylinder with this face.

4.2 Thermal Results. The analysis of the aerodynamic fields allows to validate LES and to identify the structures controlling heat transfer around the cylinders. Upstream faces of both cylinders are directly exposed to the incoming flow and are thus submitted to important heat loads. Stabilized recirculation zones on lateral faces of the upstream cylinder tend to accumulate hot fluid near the walls. On the contrary, the periodic evacuations of the lateral recirculation zones of the downstream cylinder prevent the accumulation of hot fluid. Without this protection, heat fluxes are more important. Downstream faces of the cylinders are submitted to intense turbulence leading to high heat fluxes.

To characterize convective heat transfer across the faces of the cylinders, the temporal mean Nusselt number $\overline{\mathrm{Nu}}$ is used:

$$\overline{\mathrm{Nu}} = \frac{\bar{q}_{\mathrm{wall}} D}{\lambda_{\mathrm{wall}}(T_{\mathrm{wall}} - T_\infty)} \tag{4}$$

where the temporal mean heat flux $\bar{q}_{\mathrm{wall}}$ is obtained from the Fourier law at the wall $\bar{q}_{\mathrm{wall}} = -\lambda_{\mathrm{wall}}(\partial\bar{T}/\partial n)|_{\mathrm{wall}}$.

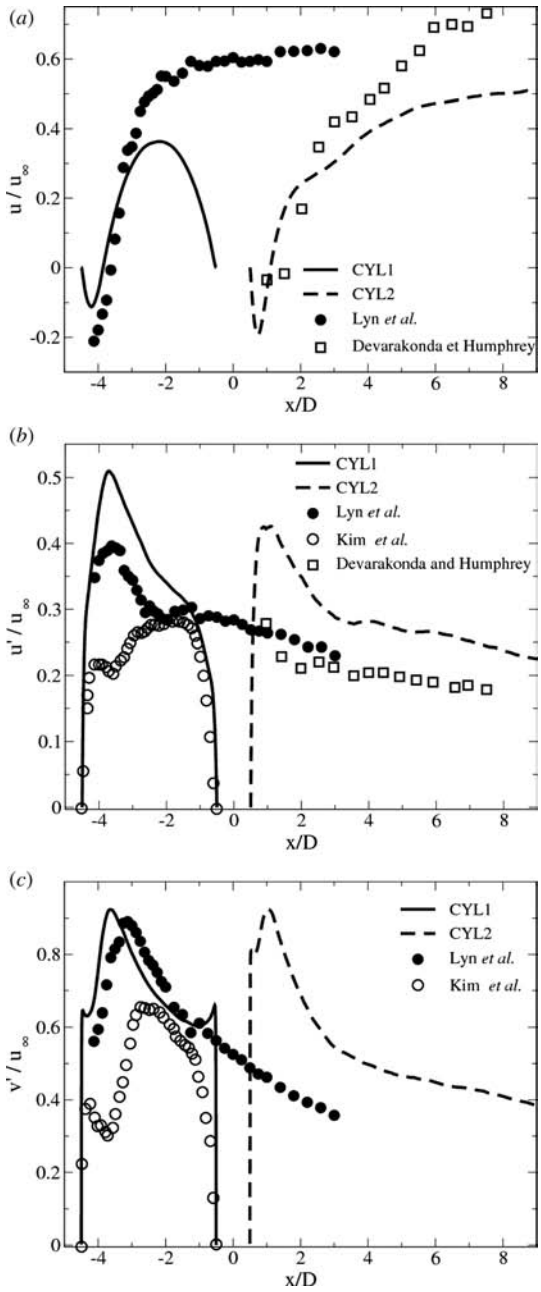

Fig. 12 (*a*) Longitudinal profiles of time-averaged streamwise velocity, $\bar{u}/U_\infty$, in the wake of the cylinders (cut *Y*0 of Fig. 3). Longitudinal profiles of time-averaged streamwise, u'/U_∞ (*b*), and transverse, v'/U_∞ (*c*), velocity fluctuations in the wake of the cylinders. Comparison with experimental data measure on an isolated cylinder [2] and on a tandem [8,14].

Figure 13 depicts mean Nusselt profiles on the upstream cylinder compared to the experimental results of Refs. [4] and [5] obtained on isolated cylinders. Experimental results are scaled following the correlation of Igarashi [4]:

$$\mathrm{Nu_S}(x) = \mathrm{Nu_E}(x)\left(\frac{\mu_\infty}{\mu_{\mathrm{wall}}}\right)^{0.14}\left(\frac{\mathrm{Re_{LES}}}{\mathrm{Re_E}}\right)^{0.66} \quad (5)$$

where μ_∞ is the dynamic viscosity of the fluid of the upstream flow, $\mathrm{Nu_E}(x)$ is the experimental measurement of the local Nusselt number at Reynolds number $\mathrm{Re_E}$, $\mathrm{Re_{LES}}$ is the Reynolds number of the LES and $\mathrm{Nu_S}(x)$ is the scaled Nusselt profile. The Nusselt

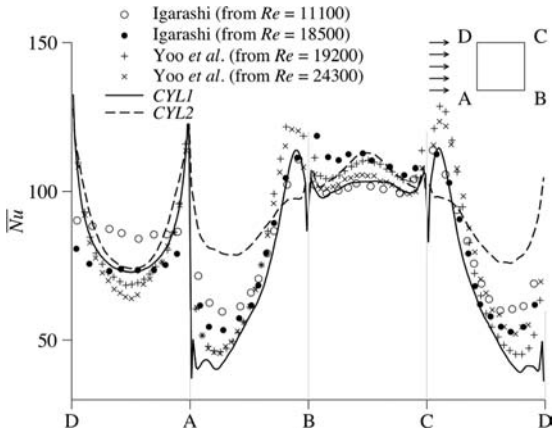

Fig. 13 Time-averaged profiles of wall Nusselt number $\overline{\mathrm{Nu}}$, profiles around the cylinder walls: Comparison between the cylinders of the LES and experiments on isolated cylinders [4,5] scaled with Eq. (5)

Table 5 Spatially and temporally averaged wall flux $\bar{\Phi}$, Nusselt number $\overline{\mathrm{Nu}}$

	$\bar{\Phi}$	$\overline{\mathrm{Nu}}$	Nu'	$\mathrm{Nu}'/\overline{\mathrm{Nu}}$
Correlation [4]	—	82.5	—	—
LES CYL 1	3.9 W	77.2	3.2	4.2%
LES CYL 2	4.5 W	89.6	9.4	10.5%

distribution of the upstream cylinder is characteristic of an isolated cylinder in terms of shape and levels.

Figure 13 shows a comparison between the Nusselt profiles of the upstream and downstream cylinders. No experimental data is available for this case but the comparison of the LES results is interesting: The cylinders exhibit differences in heat transfer due to the topology of the flow. First, the heat fluxes on the upstream face (A-D) of the cylinders are almost the same but the downstream faces (B-C) are subject to the highest heat fluxes over the whole geometry. On this face, the heat flux of the second cylinder is more important due to the closer proximity of the recirculation zone behind the obstacle evidenced by the aerodynamic analysis. The thermal effect of the presence or not of the lateral recirculation zones (faces A-B and C-D) is clearly identified in Fig. 13: The Nusselt number is very low on these faces for the upstream cylinder while it is rather high on the downstream cylinder. Finally, the shapes of the Nusselt profiles on lateral faces present an important difference near the downstream edges (B and C): There is a peak just before the edges on the profiles corresponding to the upstream cylinder replaced by a constant value for the downstream cylinder. These peaks for the upstream cylinder are due to the interaction of the shear layers with the lateral faces evidenced by the analysis of the friction (Fig. 9).

Table 5 gives global heat fluxes and Nusselt numbers integrated on the upstream and downstream cylinders as well as the root mean square values of the Nusselt numbers. The heat flux of the downstream cylinder is about 15% higher than the heat flux of the first cylinder ($\bar{\Phi}_2 \approx 1.15\bar{\Phi}_1$ and $\overline{\mathrm{Nu}}_2 \approx 1.16\,\overline{\mathrm{Nu}}_1$). Immersed in the wake of the upstream cylinder, the second cylinder also exhibits the highest temporal heat flux oscillations. The RMS value of the Nusselt number of the first cylinder is about 4.2% of $\overline{\mathrm{Nu}}_1$ while the fluctuations on the second cylinder are of the order of 10.5% of $\overline{\mathrm{Nu}}_2$. It is worth mentioning that the mean temperatures in the volumes #1 and #2 defined on Fig. 1 are approximately the same (0.5 K difference due to the mixing of the heated flow with the main flow). The corresponding mean velocity in volumes #1 and #2 are 32.5 ms^{-1} for the upstream cylinder and 26.35 ms^{-1}

for the downstream one so two opposite effects play an important role in the heat load of the downstream obstacle: (1) A reduction of the mean velocity seen by the cylinder can potentially reduce the Nusselt number, (2) an increase of velocity fluctuations can lead to an increase of heat transfer. In the configuration simulated during this study, the wake of the upstream cylinder increases the heat transfer of the second cylinder of more than 15% compared to an isolated cylinder.

5 Conclusion

This paper presents a LES of flow and heat transfer in a tandem configuration of two square cylinders at moderate Reynolds number ($\mathrm{Re} = 16,000$). LES on an unstructured mesh is used to predict the flow structure and the heat transfer at the wall. The hybrid mesh contains tetrahedra in the whole domain except in the boundary layers of the cylinder that are discretized with layers of prisms. The meshing strategy allows to resolve the flow field down to the viscous sublayer at a lower price than with only tetrahedra. Aerodynamics results are validated with experimental measurements performed on isolated cylinders and on different tandem configurations. The main flow structures responsible for heat transfer are analyzed. Finally, heat transfer around both cylinders of the tandem configuration is described. As far as aerodynamics and heat transfer are concerned, it is shown that the upstream cylinder behaves almost like an isolated cylinder. On the other hand, the wake of this first cylinder has an important impact on the second one. The analysis of the flow highlights two conflicting effects of the wake that play an important role in the heat load of the downstream obstacle: (1) A reduction of the mean velocity seen by the cylinder which reduces the Nusselt number, (2) an increase of velocity fluctuations which can lead to an increase of heat transfer. In the configuration simulated here, the second effect is preponderant.

Acknowledgment

The authors gratefully acknowledge the "Centre Informatique National de l'Enseignement Supérieur" (CINES) located in Montpellier, France for access to its computing facilities.

Nomenclature

Acronyms

- CFL = Courant–Friedrichs–Lewy number
- CYL = cylinder
- DNS = direct numerical simulation
- IC = isolated cylinder
- LES = large eddy simulation
- SGS = subgrid scale
- WALE = wall adapting local eddy

Variables

- c = speed of sound
- c_p = fluid heat capacity at constant pressure
- C_f = friction coefficient
- C_p = pressure coefficient
- D = diameter of the cylinders
- E = length of the cylinders
- h = channel height
- L = channel length
- M = Mach number
- Nu = Nusselt number
- p = pressure
- Pr = Prandtl number
- q = heat flux
- Re = Reynolds number
- s = interspace between the cylinders
- St = Strouhal number
- T = temperature
- u = axial velocity
- u_h = velocity of the nearest fluid point to the wall
- u_τ = friction velocity
- v = transverse velocity
- y^+ = wall Reynolds number
- Δh = height of the inner wall prism layer
- Δt = time step
- Δx = grid size
- λ = thermal conductivity
- μ = dynamic viscosity
- ν = kinematic viscosity
- ρ = density
- τ_wall = wall shear stress
- Φ = wall heat flux

Subscripts/Superscripts

- E = experimental quantity
- f = film quantity
- LES = LES quantity
- s = scaled quantity
- t = turbulent quantity
- wall = wall quantity
- ∞ = upstream quantity
- $\overline{\mathcal{F}}$ = time average of quantity $\mathcal{F}$
- $\mathcal{F}'$ = root mean square of quantity $\mathcal{F}$
- 1 = upstream cylinder quantity
- 2 = downstream cylinder quantity

References

[1] Bearman, P., and Obasaju, E., 1982, "An Experimental Study of Pressure Fluctuations on Fixed and Oscillating Square-Section Cylinders," J. Fluid Mech., **119**, pp. 297–321.

[2] Lyn, D. A., and Rodi, W., 1994, "The Flapping Shear Layer Formed by Flow Separation From the Forward Corner of a Square Cylinder," J. Fluid Mech., **267**, pp. 353–376.

[3] Lyn, D. A., Einav, S., Rodi, W., and Park, J., 1995, "A Laser-Doppler Velocimetry Study of Ensemble-Averaged Characteristics of the Turbulent Near Wake of a Square Cylinder," J. Fluid Mech., **304**, pp. 285–319.

[4] Igarashi, T., 1985, "Heat Transfer From a Square Prism to an Air Stream," Int. J. Heat Mass Transfer, **28**(1), pp. 175–181.

[5] Yoo, S., Park, J., Chung, C., and Chung, M., 2003, "An Experimental Study on Heat/Mass Transfer From a Rectangular Cylinder," ASME J. Heat Transfer, **125**(6), pp. 1163–1169.

[6] Takeuchi, T., and Matsumoto, M., 1992, "Aerodynamic Response Characteristics of Rectangular Cylinders in Tandem Arrangement," J. Wind Eng. Ind. Aerodyn., **41**, pp. 565–576.

[7] Haniu, H., Obata, Y., and Sakamoto, H., 1987, "Fluctuating Forces Acting on Two Square Prisms in a Tandem Arrangement," J. Wind Eng. Ind. Aerodyn., **26**, pp. 85–103.

[8] Devarakonda, R., and Humphrey, J., 1996, "Experimental Study of Turbulent Flow in the Near Wakes of Single and Tandem Prisms," Int. J. Heat Fluid Flow, **17**(3), pp. 219–227.

[9] Luo, S., Li, L., and Shah, D., 1999, "Aerodynamic Stability of the Downstream of Two Tandem Square-Section Cylinders," J. Wind Eng. Ind. Aerodyn., **79**(1–2), pp. 79–103.

[10] Liu, C.-H., and Chen, J. M., 2002, "Observations of Hysteresis in Flow Around Two Square Cylinders in a Tandem Arrangement," J. Wind Eng. Ind. Aerodyn., **90**(9), pp. 1019–1050.

[11] Alam, M. M., Moriya, M., Takai, K., and Sakamoto, H., 2002, "Suppression of Fluid Forces Acting on Two Square Prisms in a Tandem Arrangement by Passive Control of Flow," J. Fluids Struct., **16**(8), pp. 1073–1092.

[12] Zhang, P. F., Wang, J. J., Lu, S. F., and Mi, J., 2005, "Aerodynamic Characteristics of a Square Cylinder With a Rod in a Staggered Arrangement," Exp. Fluids, **38**(4), pp. 494–502.

[13] Tatsutani, K., Devarakonda, R., and Humphrey, J., 1993. "Unsteady Flow and Heat Transfer for Cylinder Pairs in a Channel," Int. J. Heat Mass Transfer, **36**(13), pp. 3311–3328.

[14] Kim, M. K., Kim, D. K., Yoon, S. H., and Lee, D. H., 2008, "Measurements of the Flow Fields Around Two Square Cylinders in a Tandem Arrangement," J. Mech. Sci. Technol., **22**(2), pp. 397–407.

[15] Rosales, J., Ortega, A., and Humphrey, J., 2001, "A Numerical Simulation of the Convective Heat Transfer in Confined Channel Flow Past Square Cylinders: Comparison of Inline and Offset Tandem Pairs," Int. J. Heat Mass Transfer, **44**(3), pp. 587–603.

[16] Sohankar, A., and Etminan, A., 2009, "Forced-Convection Heat Transfer From Tandem Square Cylinders in Cross Flow at Low Reynolds Numbers," Int. J. Numer. Methods Fluids, **60**(7), pp. 733–751.

[17] Chatterjee, D., and Amiroudine, S., 2010, "Two-Dimensional Mixed Convection Heat Transfer From Confined Tandem Square Cylinders in Cross-Flow at low Reynolds Numbers," Int. Commun. Heat Mass Transfer, **37**(1), pp. 7–16.
[18] Sagaut, P., 2000, *Large Eddy Simulation for Incompressible Flows* (Scientific Computation Series), Springer-Verlag, Heidelberg.
[19] Moin, P., 2002, "Advances in Large Eddy Simulation Methodology for Complex Flows," Int. J. Heat Fluid Flow, **23**(5), pp. 710–720.
[20] Poinsot, T., and Veynante, D., 2005, *Theoretical and Numerical Combustion*, 2nd ed., R. T. Edwards, Inc.
[21] Boudier, G., Gicquel, L. Y. M., Poinsot, T., Bissières, D., and Bérat, C., 2007, "Comparison of LES, RANS and Experiments in an Aeronautical Gas Turbine Combustion Chamber," Proc. Combust. Inst., **31**(2), pp. 3075–3082.
[22] Duchaine, F., Corpron, A., Pons, L., Moureau, V., Nicoud, F., and Poinsot, T., 2009, "Development and Assessment of a Coupled Strategy for Conjugate Heat Transfer With Large Eddy Simulation. Application to a Cooled Turbine Blade," Int. J. Heat Fluid Flow, **30**(6), pp. 1129–1141.
[23] Bricteux, L., Duponcheel, M., and Winckelmans, G., 2009, "A Multiscale Subgrid Model for Both Free Vortex Flows and Wall-Bounded Flows," Phys. Fluids, **21**(10), p. 105102.
[24] Lamarque, N., Zoppé, B., Lebaigue, O., Dolias, Y., Bertrand, M., and Ducros, F., 2010, "Large-Eddy Simulation of the Turbulent Free-Surface Flow in an Unbaffled Stirred Tank Reactor," Chem. Eng. Sci., **65**(15), pp. 4307–4322.
[25] Ferziger, J. H., and Perić, M., 1997, *Computational Methods for Fluid Dynamics*, Springer-Verlag, Berlin.
[26] Smagorinsky, J., 1963, "General Circulation Experiments With the Primitive Equations: 1. The Basic Experiment.," Mon. Weather Rev., **91**, pp. 99–164.
[27] Pope, S. B., 2000, *Turbulent Flows*, Cambridge University, Cambridge, UK.
[28] Nicoud, F., and Ducros, F., 1999, "Subgrid-Scale Stress Modeling Based on the Square of the Velocity Gradient," Flow, Turbine Combust., **62**(3), pp. 183–200.
[29] Schönfeld, T., and Poinsot, T., 1999, "Influence of Boundary Conditions in LES of Premixed Combustion Instabilities," Annual Research Briefs, Center for Turbulence Research, NASA Ames/Stanford University, pp. 73–84.
[30] Roux, A., Gicquel, L. Y. M., Sommerer, Y., and Poinsot, T. J., 2008, "Large Eddy Simulation of Mean and Oscillating Flow in a Side-Dump Ramjet Combustor," Combust. Flame, **152**(1–2), pp. 154–176.
[31] Boileau, M., Duchaine, F., Poinsot, T., and Sommerer, Y., 2013, "Large Eddy Simulation of Heat Transfer Around a Square Cylinder," Am. Inst. Aeronaut. Astronaut. J., **51**(2), pp. 372–385.
[32] Donea, J., and Huerta, A., 2003, *Finite Element Methods for Flow Problems*, Wiley, New York.
[33] Colin, O., and Rudgyard, M., 2000, "Development of High-Order Taylor–Galerkin Schemes for Unsteady Calculations," J. Comput. Phys., **162**(2), pp. 338–371.
[34] Sheard, G. J., Fitzgerald, M. J., and Ryan, K., 2009, "Cylinders With Square Cross-Section: Wake Instabilities With Incidence Angle Variation," J. Fluid Mech., **630**, pp. 43–69.
[35] Poinsot, T., and Lele, S., 1992, "Boundary Conditions for Direct Simulations of Compressible Viscous Flows," J. Comput. Phys., **101**(1), pp. 104–129.
[36] Jeong, J., and Hussain, F., 2005, "On the Identification of a Vortex," J. Fluid Mech., **285**, pp. 308–323.